X-ray polarimetry of X-ray pulsar X Persei: another orthogonal rotator?

A. A. Mushtukov [1,2]⋆ S. S. Tsygankov [3] J. Poutanen [3] V. Doroshenko [4] A. Salganik [5,6]
E. Costa,[7] A. Di Marco [7] J. Heyl [8] F. La Monaca [7] A. A. Lutovinov,[6] I. A. Mereminsky [6]
A. Papitto,[9] A. N. Semena,[6] A. E. Shtykovsky,[6] V. F. Suleimanov [4] S. V. Forsblom [3]
D. González-Caniulef [10] C. Malacaria [11] R. A. Sunyaev,[6,12] I. Agudo,[13] L. A. Antonelli,[14,15]
M. Bachetti,[16] L. Baldini,[17,18] W. H. Baumgartner,[19] R. Bellazzini,[17] S. Bianchi,[20] S. D. Bongiorno,[19]
R. Bonino,[21,22] A. Brez,[17] N. Bucciantini,[23,24,25] F. Capitanio,[7] S. Castellano,[17] E. Cavazzuti,[26]
C.-T. Chen,[27] S. Ciprini,[15,28] A. De Rosa,[7] E. Del Monte,[7] L. Di Gesu,[26] N. Di Lalla,[29] I. Donnarumma,[26]
M. Dovčiak,[30] S. R. Ehlert,[19] T. Enoto,[31] Y. Evangelista,[7] S. Fabiani,[7] R. Ferrazzoli,[7] J. A. Garcia,[32]
S. Gunji,[33] K. Hayashida,[34]† W. Iwakiri,[35] S. G. Jorstad,[36,37] P. Kaaret,[19] V. Karas,[30] F. Kislat,[38]
T. Kitaguchi,[31] J. J. Kolodziejczak,[19] H. Krawczynski,[39] L. Latronico,[21] I. Liodakis,[40] S. Maldera,[21]
A. Manfreda,[41] F. Marin,[42] A. P. Marscher,[36] H. L. Marshall,[43] F. Massaro,[21,22] G. Matt,[20] I. Mitsuishi,[44]
T. Mizuno,[45] F. Muleri,[7] M. Negro,[46,47,48] C.-Y. Ng,[49] S. L. O'Dell,[19] N. Omodei,[29] C. Oppedisano,[21] G.
G. Pavlov,[50] A. L. Peirson,[29] M. Perri,[14,15] M. Pesce-Rollins,[17] P.-O. Petrucci,[51] M. Pilia,[16] A. Possenti,[16]
S. Puccetti,[15] B. D. Ramsey,[19] J. Rankin,[7] A. Ratheesh,[7] O. J. Roberts,[27] R. W. Romani,[29] C. Sgrò,[17]
P. Slane,[52] P. Soffitta,[7] G. Spandre,[17] D. A. Swartz,[27] T. Tamagawa,[31] F. Tavecchio,[53] R. Taverna,[54]
Y. Tawara,[44] A. F. Tennant,[19] N. E. Thomas,[19] F. Tombesi,[28,55,56] A. Trois,[16] R. Turolla,[54,57] J. Vink,[58]
M. C. Weisskopf,[19] K. Wu,[57] F. Xie[7,59] and S. Zane[57]

Affiliations are listed at the end of the paper

ABSTRACT

X Persei is a persistent low-luminosity X-ray pulsar of period of ≈ 835 s in a Be binary system. The field strength at the neutron star surface is not known precisely, but indirect signs indicate a magnetic field above 10^{13} G, which makes the object one of the most magnetized known X-ray pulsars. Here we present the results of observations X Persei performed with the *Imaging X-ray Polarimetry Explorer* (*IXPE*). The X-ray polarization signal was found to be strongly dependent on the spin phase of the pulsar. The energy-averaged polarization degree in 3–8 keV band varied from several to ~ 20 per cent over the pulse with a phase dependence resembling the pulse profile. The polarization angle shows significant variation and makes two complete revolutions during the pulse period, resulting in nearly nil pulse-phase averaged polarization. Applying the rotating vector model to the *IXPE* data we obtain the estimates for the rotation axis inclination and its position angle on the sky, as well as for the magnetic obliquity. The derived inclination is close to the orbital inclination, reported earlier for X Persei. The polarimetric data imply a large angle between the rotation and magnetic dipole axes, which is similar to the result reported recently for the X-ray pulsar GRO J1008−57. After eliminating the effect of polarization angle rotation over the pulsar phase using the best-fitting rotating vector model, the strong dependence of the polarization degree with energy was discovered, with its value increasing from 0 at ~ 2 keV to 30per cent at 8 keV.

Key words: magnetic fields – polarization – stars: neutron – stars: oscillations – pulsars: individual: X Persei – X-rays: binaries.

1 INTRODUCTION

Accretion of matter on to spinning and strongly magnetized neutron stars (NSs) in close binary systems results in a phenomenon of X-ray pulsars (XRPs, see Mushtukov & Tsygankov 2022 for review). The magnetic field strength at the NS surface in XRPs is typically measured to be $\sim 10^{12}$ G, and in some sources is confirmed to be as high as $\sim 10^{13}$ G (Staubert et al. 2019; Kong et al. 2022). Such a strong magnetic field affects both geometry of the accretion flow in XRPs and the physical processes of interaction between radiation and matter (Harding & Lai 2006; Suleimanov et al. 2022), making XRPs unique labs to study physics under extreme conditions.

The geometry of the emitting regions in XRPs is known to be dependent on the mass accretion rate (Basko & Sunyaev 1976): at relatively low mass accretion rates ($\dot{M} \lesssim 10^{17}\,\mathrm{g\,s^{-1}}$), the accretion flow is decelerated in the atmosphere of a NS (Zel'dovich & Shakura 1969), while a high mass accretion rate ($\dot{M} \gtrsim 10^{17}\,\mathrm{g\,s^{-1}}$) results in the appearance of a radiation dominated shock above the NS surface and extended accretion columns confined by a strong magnetic field, and supported vertically by the radiation pressure (Basko & Sunyaev 1976; Wang & Frank 1981).

The influence of the strong magnetic field on the radiative transfer in the NS atmospheres has long been discussed in the literature. In particular, it is well known that the transfer of radiation critically depends on the polarization of X-ray photons and the direction of their propagation, with respect to the local direction of magnetic field (see Gnedin & Pavlov 1974; Kaminker, Pavlov & Shibanov 1983 and Chapter 6 in Meszaros 1992 for review). Most of the existing models (Meszaros & Nagel 1985a, b; Caiazzo & Heyl 2021; Sokolova-Lapa et al. 2021) predict a degree of linear polarization up to 80 per cent at energies below the cyclotron resonance (i.e. at $E < E_{\mathrm{cyc}} \approx 11.6\,B_{12}$ keV, where $B_{12} = B/10^{12}$ G is the local magnetic field strength). This makes XRPs one of the main targets for the new generation of X-ray polarimeters.

Thanks to the first highly sensitive space X-ray polarimeter, the *Imaging X-ray Polarimeter Explorer* (*IXPE*, Weisskopf et al. 2022), polarization in X-ray energy band has been discovered in XRPs Her X-1 (Doroshenko et al. 2022), Cen X-3 (Tsygankov et al. 2022), GRO J1008−57 (Tsygankov et al. 2023), and Vela X-1 (Forsblom et al. 2023). Detection of polarization in the X-ray energy band allowed to determine the geometrical parameters of the NS, and obtain constraints of the magnetic field structure and the structure of the NS atmosphere. Unexpectedly, the observed polarization degree (PD) below 10–15 per cent, even in the phase-resolved data, turned out to be much smaller than that predicted by most theoretical models. To understand the nature of this discrepancy, we need to observe sources with very different parameters determining geometrical and physical conditions of the emission region.

X Persei (4U 0352+309) belongs to the rare class of persistent low-luminosity XRPs, with Be optical companions (e.g. Reig & Roche 1999). Pulsations of the flux with a period of 835 s were discovered from the source, with the *Copernicus* satellite (White et al. 1976). The pulsar moves around its optical companion, star HD 24534, along a moderately eccentric ($e = 0.11 \pm 0.02$) wide orbit with a period of $P_{\mathrm{orb}} = 250.3 \pm 0.6$ d, orbital inclination $i_{\mathrm{orb}} \approx 30°$, a projected semimajor axis of the NS of $a_x \sin i = 454 \pm 4$ lt-s, and the mass function $f(M) = 1.61 \pm 0.05\,\mathrm{M_\odot}$ (Delgado-Martí et al. 2001). Additional quasi-periodic variations of the observed flux from the source with a period of about seven years were reported by Nakajima et al. (2019). Recently, the most accurate distance to X Persei of 600 ± 13 pc was determined from the *Gaia* Early Data Release 3 (Bailer-Jones et al. 2021). The magnetic field of the NS in X Persei is not known precisely, but all estimates including broad-band X-ray spectral analyses and the observed evolution of spin frequency point to high magnetic field values. In particular, a wide depression in the source spectrum observed at around 30 keV was interpreted by Coburn et al. (2001) and Lutovinov, Tsygankov & Chernyakova (2012) as a cyclotron resonant scattering feature, equivalent to a magnetic field strength of $\approx 2.5 \times 10^{12}$ G. However, this spectral feature was later proposed to be related to the double-hump continuum shape typical to XRPs, at extremely low mass accretion rates (Tsygankov et al. 2019a). This would shift the magnetic field to even higher values: $\gtrsim 10^{13}$ G (e.g. Di Salvo et al. 1998; Tsygankov et al. 2019b; Mushtukov et al. 2021; Sokolova-

Lapa et al. 2021). Applying the accretion torque models to the spin frequency evolution of the source, another estimate of the magnetic field strength can be obtained: $B \sim 4 \times 10^{13} - 2.5 \times 10^{14}$ G (Doroshenko et al. 2012; Yatabe et al. 2018), which supports the estimate made from the source spectral shape. Combination of a strong magnetic field and low mass accretion rate in X Persei point to the accretion from cold disc composed of recombined material (see, e.g. Tsygankov et al. 2017).

X Persei is the closest low luminosity ($L \sim 10^{35}\,\mathrm{erg\,s^{-1}}$) pulsar known, which provides a unique opportunity to study accretion at low rates, with good counting statistics essential for polarimetric observations. Furthermore, the low mass accretion rate in this object implies that it must have a simple geometrical configuration of the emitting regions at the NS surface, so called hotspot, which simplifies interpretation of the results. The magnetic field of X Persei is strong, even by the standards of XRPs and makes the source particularly interesting for polarimetric observations, as the energy range covered by *IXPE* is much below the cyclotron energy, which again simplifies theoretical interpretation of the results.

Here we present the results of *IXPE* observations of X Persei, performed in 2022 August and September. In Section 2, we present the *IXPE* data as well as the accompanying observations by *SRG*/ART-XC. Section 3 is devoted to the results of the X-ray polarimetric observations. We discuss the structure of the atmosphere and the constraints obtained on the geometry in Section 4, and we summarize our findings in Section 5.

2 DATA

2.1 *IXPE*

X Persei was observed with *IXPE* over the periods of 2022 Aug 19–22 and Sep 16–19, with a total effective exposure of $\simeq 225$ ks. *IXPE* is a joint effort of NASA and the Italian Space Agency, launched by a Falcon 9 rocket on 2021 December 9. The observatory consists of three grazing incidence telescopes, each equipped with an X-ray mirror assembly and a polarization-sensitive detector unit (DU) (Baldini et al. 2021; Soffitta et al. 2021). It provides imaging polarimetry over a nominal 2–8 keV band. The time resolution and accuracy is $< 10\,\mu$s, far better than what is needed for our analysis. A detailed description of the instrument and its performance is given in Weisskopf et al. (2022).

The data have been processed with the publicly available IXPEOB-SSIM package[1] version 30.2.2 (Baldini et al. 2022), using CALDB released on 2022 November 17. Source photons were collected in a circular region with radius $R_{\mathrm{src}} = 60$ arcsec, centred on the X Persei position. Following recommendations from Di Marco et al. (2023) for bright sources, the background was not subtracted from the data, because it appears to be negligible (~ 1 per cent of the total signal). The event arrival times were corrected to the Solar system barycentre, using the standard BARYCORR tool from the FTOOLS package and accounting for the effects of binary motion, using the orbital parameters by Delgado-Martí et al. (2001). The resulting light curve of X Persei in the 2–8 keV band is shown in the upper panel of Fig. 1. Because the source does not demonstrate significant difference in the average count rate in the two observational segments, the subsequent scientific analysis was performed using the joint data set.

The same extraction procedure was applied to all three Stokes parameters I, Q, and U. In order to use the χ^2 statistics, the

---

[1] https://github.com/lucabaldini/ixpeobssim
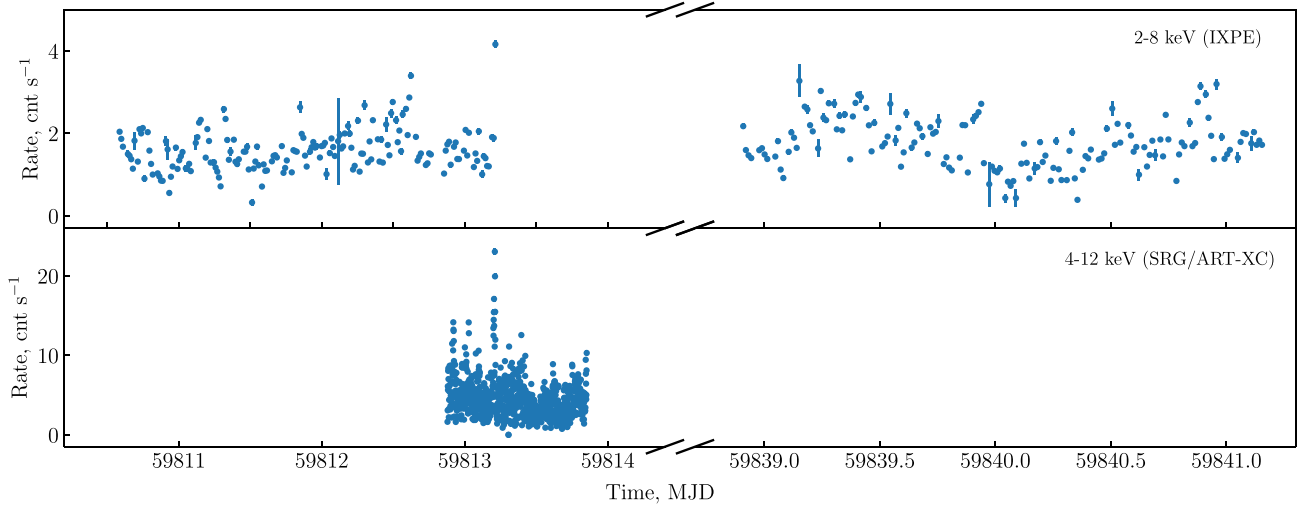
Figure 1. *Top:* The light curve of X Persei in the 2–8 keV energy band summed over three modules of *IXPE*. Both observations performed in 2022 Aug and Sep are shown. *Bottom:* The light curve of the source in the 4–12 keV band obtained during the quasi-simultaneous *SRG*/ART-XC observation.

flux (Stokes parameter *I*) energy spectra were rebinned to have at least 30 counts per energy channel. The energy binning obtained for the Stokes parameter *I* was also applied to the spectra of the Stokes parameters *Q* and *U*. The subsequent spectral fitting was performed with the XSPEC package (Arnaud 1996) using the latest version 12 of *IXPE* response matrices, available on the IXPEOBSSIM public repository.[2] Taking into account the high count statistic and negligible background level, the unweighted approach has been applied. The uncertainties are given at the 68.3 per cent confidence level for a single parameter of interest, unless stated otherwise.

2.2 *SRG*/ART-XC

To control the temporal and spectral properties of X Persei in the broader energy band, the quasi-simultaneous observations with the *Spectrum-Roentgen-Gamma observatory* (*SRG*, Sunyaev et al. 2021) and Mikhail Pavlinsky *ART-XC telescope* (Pavlinsky et al. 2021) were carried out on MJD 59813, with an ∼84 ks net exposure. The *ART-XC telescope* includes seven independent modules and provides imaging, timing, and spectroscopy in the 4–30 keV energy range. *ART-XC* data were processed with the analysis software ARTPRODUCTS v1.0 and the CALDB version 20220908. The corresponding light curves of X Persei in the 4–24 keV band are shown in the lower panels of Fig. 1.

3 RESULTS

Considering that the main goal of our investigation is pulse-phase resolved spectro-polarimetric analysis, we first determined pulsation period for the period covered by *IXPE* data. The pulse period was determined as 833.14(1) s, using the event data (with event arrival times corrected for effects of orbital motion of the satellite and NS as described above) and Z^2 statistics (Buccheri et al. 1983). The folded pulse profile in different energy bands based on the *IXPE* and *ART-XC* data (see Fig. 2) demonstrates a typical shape for the source, with only minor dependence on energy.

Following standard procedures for *IXPE* data analysis of XRPs (Doroshenko et al. 2022; Tsygankov et al. 2022), we performed
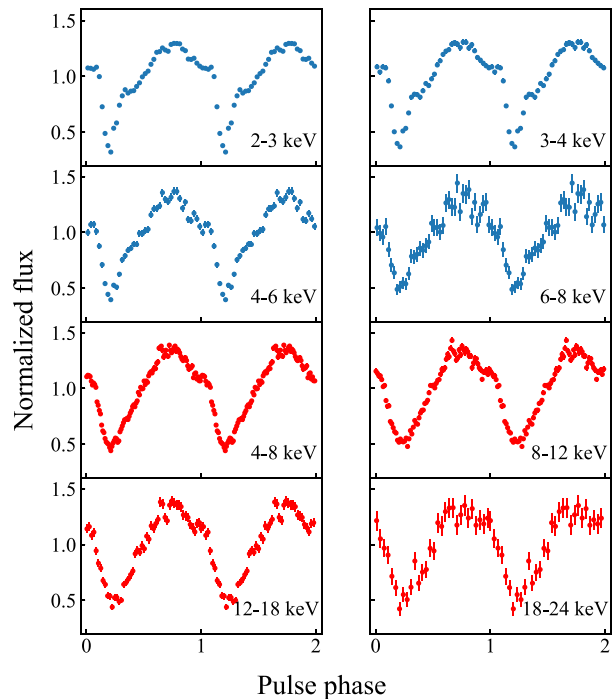
Figure 2. Pulse profile of X Persei normalized to the mean flux in different energy bands as seen by *IXPE* (upper four panels in blue) and *ART-XC telescope* (bottom four panels in red). Data from the three and seven *IXPE* and *ART-XC* units, respectively, were combined.

polarimetric analysis of the data using the formalism of Kislat et al. (2015), implemented in the PCUBE algorithm in the XPBIN tool as a part of the IXPEOBSSIM package (Baldini et al. 2022), as well as using spectro-polarimetric analysis with the the XSPEC package (Strohmayer 2017). At the first step, we explored the energy dependence of the polarimetric properties of X Persei. In the detailed spectro-polarimetric analysis presented below (see Section 4.2), we found a strong dependence of polarization on energy resulting in the undetectable polarization below 3 keV, in the pulse phase-averaged
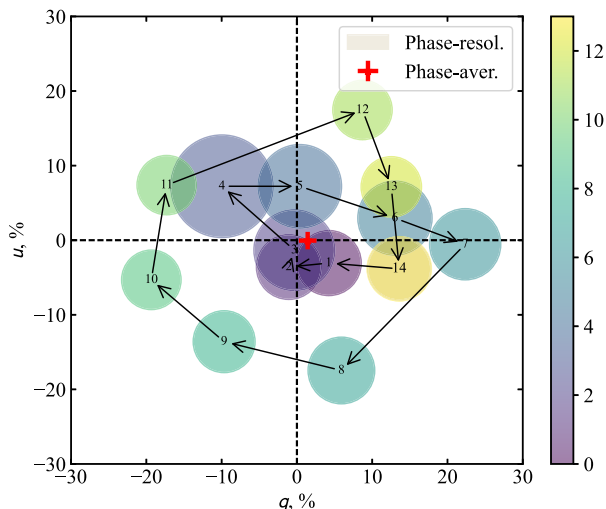
Figure 3. Variations of the phase-resolved normalized Stokes parameters $q = Q/I$ and $u = U/I$ (from using PCUBE) over the spin phase of X Persei in the 3–8 keV energy band averaged over three DUs. Colour coding and the size of the corresponding circle correspond to the phase bin number and 1σ uncertainty, respectively. The phase-averaged value is shown with the red cross.

as well as in the phase-resolved data. Therefore, to demonstrate more clearly the phase dependence of the PD and the polarization angle (PA, measured from north to east) in the energy-binned data, we excluded the 2–3 keV data from the following analysis.

Pulse-phase averaged polarimetric analysis using the PCUBE algorithm in the 3–8 keV band resulted in a very low, consistent with zero, polarization with the normalized Stokes parameters of $q = Q/I = 1.4 \pm 1.2$ and $u = U/I = 0.0 \pm 1.2$ per cent (see the red cross in Fig. 3). However, similarly to the other XRPs studied with *IXPE*, phase-resolved analysis revealed a very strong variability of q and u, over the pulse phase (Fig. 3).[3] We see that the PD $= \sqrt{q^2 + u^2}$ varies from being consistent with zero to ~ 20 per cent. The non-detection in the phase-averaged data can be thus attributed to a rotation of the PA, with the pulse phase.

At the next step, we performed spectro-polarimetric analysis with XSPEC to account for the energy dispersion and the spectral shape. We fitted jointly the I, Q, and U spectra prepared with the PHA1, pha1q, and pha1u algorithms in the XPBIN tool. To avoid problems with the mismatch in spectral calibrations of *IXPE* and *ART-XC telescopes* and the fact that observations only partly overlap, for the following analysis only data from *IXPE* were used.

The spectrum of X Persei is relatively simple and below 10 keV can be well described with an absorbed power law. The interstellar absorption was accounted for using the `tbabs` model with abundances adopted from Wilms, Allen & McCray (2000). Moreover, the fit appeared to be insensitive to the N_H value and it was fixed at 0.15×10^{22} cm^{-2} (see e.g. Di Salvo et al. 1998). The PD and PA values were derived from the `polconst` model, assuming their independence of the energy. The statistical quality of the data does not allow us to investigate the energy dependence in the phase-resolved data. A cross-calibration multiplicative constant (`const` in XSPEC) was introduced to the model in order to take into account possible

---

discrepancies in the DU's effective areas (with DU1 constant fixed to unity). The quality of the phase-averaged spectrum approximation can be seen in Fig. 4 with the best-fitting parameters presented in Table 1.

The same spectral model was applied to the phase-resolved data. All the spectral parameters were allowed to vary, except the cross-calibration constants, which were fixed to values obtained from the phase-averaged fit. The obtained results are summarized in Figs 5, 6, and Table 2. We see that the PD closely follows evolution of the pulsed flux with the pulse phase, similarly to what was recently found in another XRP, with luminosity much below the critical value, GRO J1008−57 (Tsygankov et al. 2023). The PA varies from $-90°$ to $+90°$, covering the widest range among the XRPs observed until now with *IXPE*. During the pulse period, the PA makes two complete revolutions.
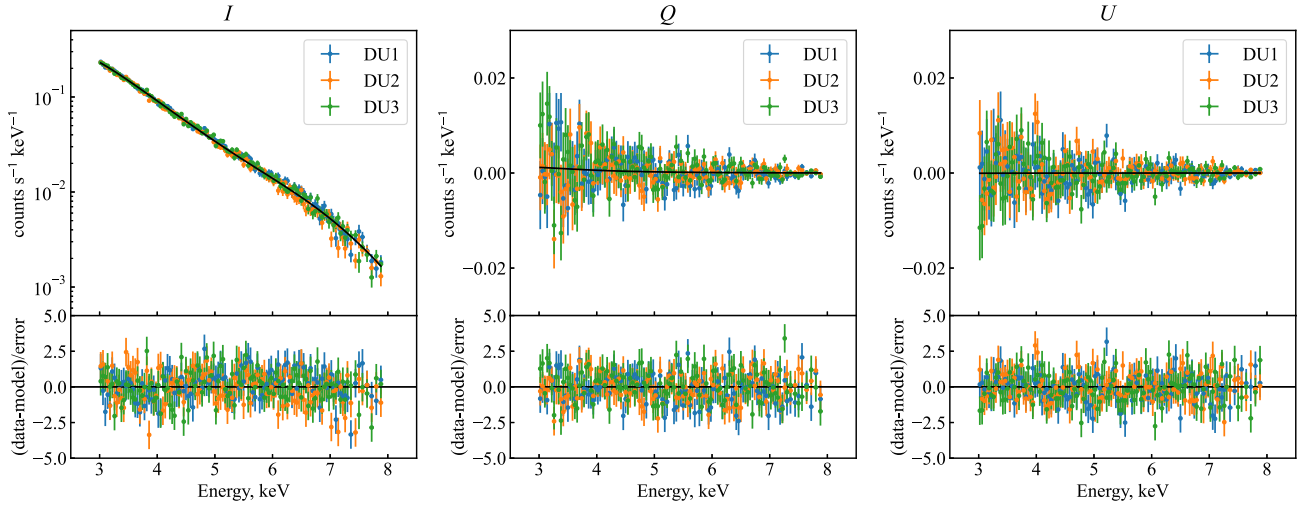
4 DISCUSSION

4.1 Atmospheric structure and polarization mechanism

We estimate the bolometric accretion luminosity of X Persei to be below $\sim 5 \times 10^{34}$ erg s^{-1}. For the surface magnetic field of about 10^{13} G, this luminosity is well below the critical value $L_{crit} \approx 3 \times 10^{37}$ erg s^{-1} (Basko & Sunyaev 1976; Mushtukov et al. 2015), above which the radiative pressure force becomes high enough to stop the accretion flow above the NS surface. Under the condition of $L \ll L_{crit}$, the influence of radiation pressure on the dynamics of the accretion flow is negligible and the accretion results in a hotspot geometry of the emission region. The two-component structure of the broad-band 4–200 keV energy spectrum as reported by Doroshenko et al. (2012), and the luminosity of X Persei indicate that the X-rays are emitted from the atmosphere under the conditions where the upper optically thin layer are overheated by the deceleration of accreting gas (Zel'dovich & Shakura 1969; Suleimanov, Poutanen & Werner 2018). In this case, the low-energy component of the X-ray spectrum is produced by the thermal emission of underlying cold atmospheric layers, while the high-energy component is shaped by the cyclotron emission and subsequent multiple Compton resonant scatterings in the hot electron gas (Mushtukov et al. 2021; Sokolova-Lapa et al. 2021).

It is expected that a NS atmosphere with an inverse temperature profile produces a pencil beam emission pattern, which is suppressed along the NS surface normal: the hot upper layers contribute more to the X-ray energy flux, leaving the NS atmosphere at larger angles with respect to the local normal. In the case of a hotspot geometry, the PD below the cyclotron resonance is expected to be higher for photons, leaving the atmosphere at larger angles to the local magnetic field direction because of a stronger dependence of scattering and absorption cross-sections on polarization (Meszaros et al. 1988). Thus, the expected correlation between the flux and the PD is in agreement with the observations (compare panels a and d in Fig. 5). It means that the minimal X-ray energy flux and the PD correspond to the smallest angle between the NS magnetic axis and the line of sight. A similar behaviour of the X-ray energy flux and the PD with the pulse phase was detected recently in GRO J1008−57, where the XRP was also observed below the critical luminosity (Tsygankov et al. 2023). An opposite behaviour was, however, found in a brighter XRP Cen X-3, accreting at around the critical rate (Tsygankov et al. 2022).

The low PD observed in X Persei is probably related to the inverse temperature profile in the NS atmosphere. The radiative transfer process in a strongly magnetized medium can be considered in

---

[3] The quoted q and u are intrinsic, i.e. corrected for the modulation amplitude. This is done within the PCUBE algorithm following prescription from Kislat et al. (2015).

Figure 4. Energy distributions of the Stokes parameters *I*, *Q*, and *U* averaged over the spin phase of X Persei, obtained with *IXPE* in the 3–8 keV band. The best-fitting model is shown with the black solid line. Bottom panels of each plot represent the residuals between the data and the model normalized for the error. Data from the three *IXPE* detectors are shown with different colours: DU1 in blue, DU2 in orange, and DU3 in green.

Table 1. Spectral parameters of the best-fitting model for the phase-averaged *IXPE* data on X Persei in the 3–8 keV band using XSPEC.

Parameter	Value	Units
N_{H}	0.15 (fixed)	10^{22} cm^{-2}
const$_{\mathrm{DU2}}$	0.95 ± 0.01	
const$_{\mathrm{DU3}}$	0.91 ± 0.01	
Photon index	1.72 ± 0.02	
PD	1.8 ± 1.0	%
PA	-1 ± 16	deg
Flux (2–8 keV)	2.76 ± 0.04	10^{-10} erg cm^{-2} s^{-1}
Luminosity (2–8 keV)	1.2×10^{34}	erg s^{-1} at $d = 600$ pc
χ^2 (degrees of freedom)	1044 (1038)	

Quoted uncertainties are at the 68.3 per cent confidence level. Systematic uncertainty of 5 per cent was added in order to obtain the reliable errors on the model parameters.

terms of propagation of two polarisation modes: X- and O-mode photons (Gnedin & Pavlov 1974). The electric vector of the X-mode photons oscillates predominantly in the direction orthogonal to the local magnetic field direction, while oscillations of electric vector of the O-mode photons have significant component along the field lines. Below the cyclotron resonance, scattering and free-free absorption coefficients tend to be larger for the photons of O-mode (Meszaros 1992). In the case of the atmosphere with the inverse temperature profile, two effects come into play. On the one hand, deep layers of the atmosphere provide X-ray flux dominated by the X-mode photons, but the upper atmosphere in local thermodynamic equilibrium emits many O-mode photons, for which the absorption and scattering cross-sections are larger. Because the emission occurs in an optically thin upper layer, these photons freely leave the atmosphere and equalize the difference between the fluxes in the two polarization modes (Mushtukov et al. 2021). In this scenario, the difference between fluxes in the two modes tend to be smaller at lower energies (see fig. 5 in Mushtukov et al. 2021). On the other hand, the estimates show that the temperature between the upper overheated layer and the lower cold atmosphere changes sharply, and there is a region with a large temperature gradient (Suleimanov et al. 2018). Under the condition of hydrostatic equilibrium, the temperature jump is
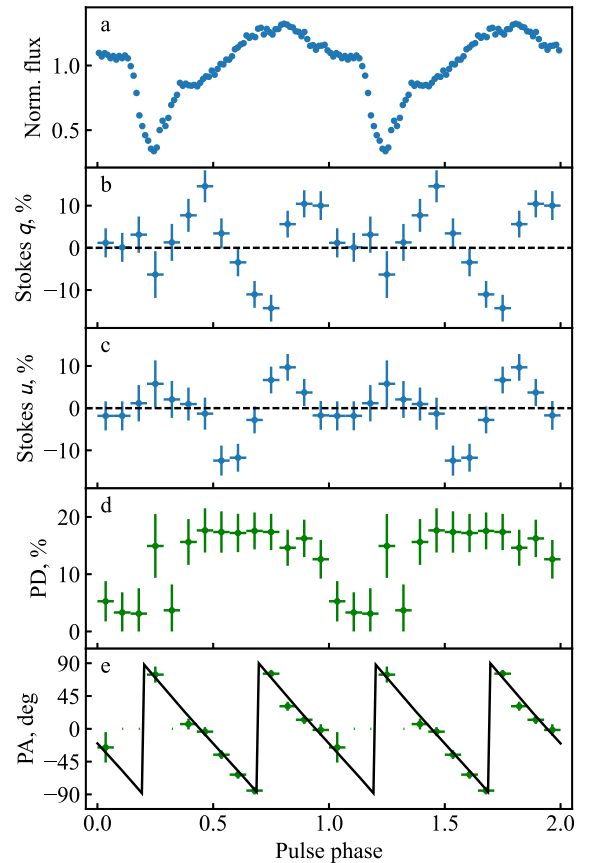
Figure 5. Dependence of the flux normalized to its mean (*panel a*), normalized $q = Q/I$, and $u = U/I$ Stokes parameters (*panels b and c*), PD and PA (*panels d and e*) on the pulse phase in the 3–8 keV energy band. Data from the three *IXPE telescopes* are combined. Data for three phase bins are missing the PA values, because they are not constrained. The black solid line in the bottom panel corresponds to the best-fitting rotating vector model (RVM), with the following parameters: $i_{\mathrm{p}} = 162°$, $\theta = 90°$, $\chi_{\mathrm{p}} = 70°$, and $\phi_0/2\pi = 0.75$.
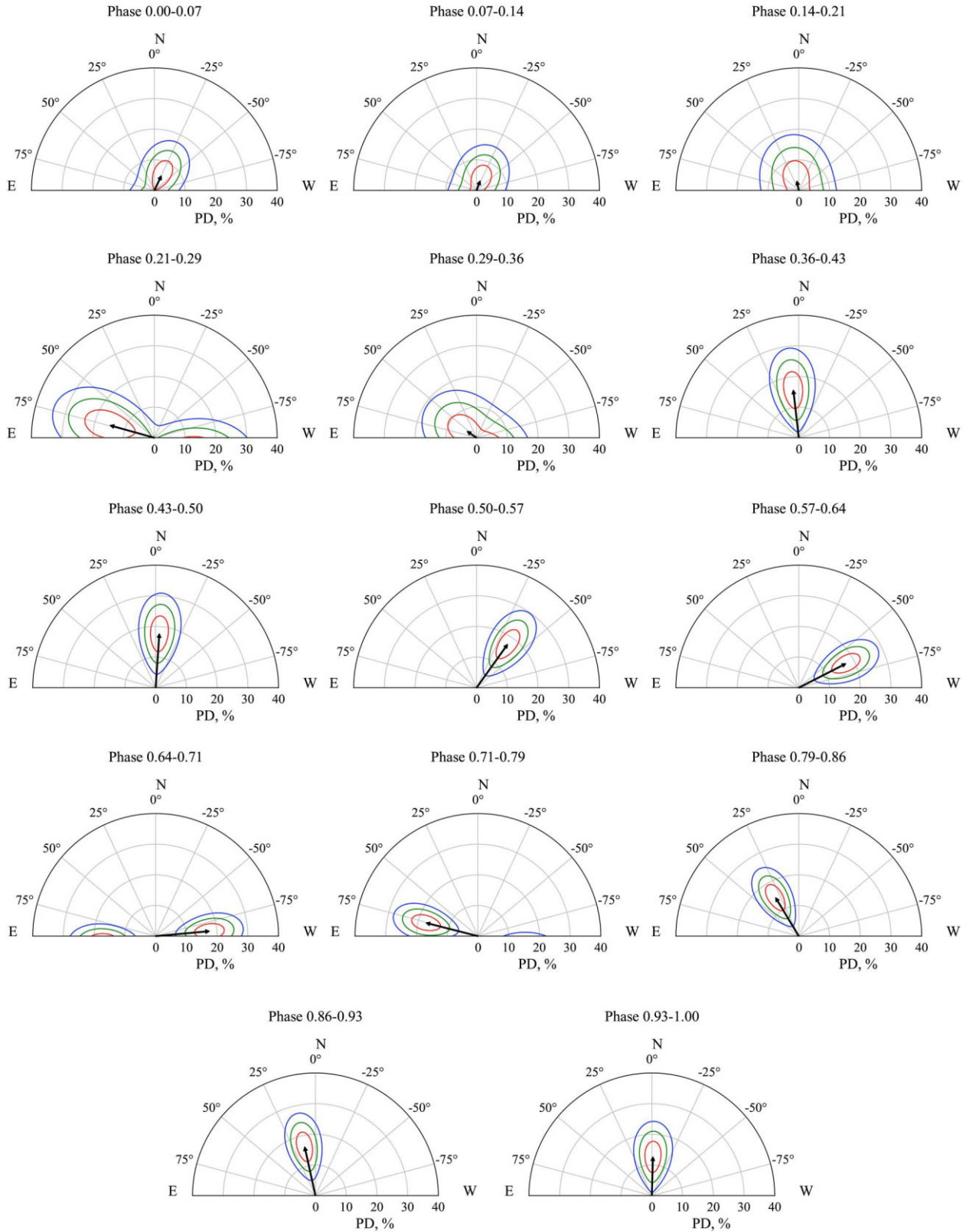
Figure 6. Polarization vector of X Persei as a function of the pulse phase based on the spectro-polarimetric analysis. The PD and PA contours at 68.27, 95.45, and 99.73 per cent confidence levels (in red, green, and blue colour, respectively) are shown in polar coordinates, for 14 phase intervals.

Table 2. Spectral parameters for the phase-resolved spectro-polarimetric analysis of the X Persei data with XSPEC.

#	Phase	Photon index	PD (per cent)	PA (deg)	χ^2 (degrees of freedom)
1	0.000–0.071	1.64 ± 0.04	5.3 ± 3.5	-25.5 ± 21.0	563 (569)
2	0.071–0.143	1.73 ± 0.04	3.3 ± 3.3	...	522 (550)
3	0.143–0.214	1.69 ± 0.04	$3.1^{+4.4}_{-3.1}$	...	501 (460)
4	0.214–0.286	1.37 ± 0.04	14.9 ± 5.6	74.4 ± 11.0	345 (362)
5	0.286–0.357	1.79 ± 0.04	$3.7^{+4.5}_{-3.7}$	...	435 (449)
6	0.357–0.429	1.70 ± 0.04	15.6 ± 4.0	6.5 ± 7.4	536 (488)
7	0.429–0.500	1.58 ± 0.04	17.6 ± 3.9	3.9 ± 6.2	545 (517)
8	0.500–0.571	1.60 ± 0.04	17.4 ± 3.6	-35.5 ± 6.0	524 (544)
9	0.571–0.643	1.67 ± 0.04	17.2 ± 3.3	-62.9 ± 5.6	667 (597)
10	0.643–0.714	1.63 ± 0.04	17.6 ± 3.2	-84.8 ± 5.3	590 (611)
11	0.714–0.786	1.56 ± 0.04	17.4 ± 3.2	75.7 ± 5.2	624 (612)
12	0.786–0.857	1.59 ± 0.04	14.6 ± 3.1	31.0 ± 6.2	666 (620)
13	0.857–0.929	1.67 ± 0.04	16.3 ± 3.3	12.4 ± 5.7	622 (602)
14	0.929–1.000	1.59 ± 0.04	12.6 ± 3.4	-1.6 ± 7.8	532 (581)

The cross-normalization constants, as well as the N_H value are frozen at the values derived from the phase-averaged analysis. The missing values of the PA correspond to non-detection of the polarization.
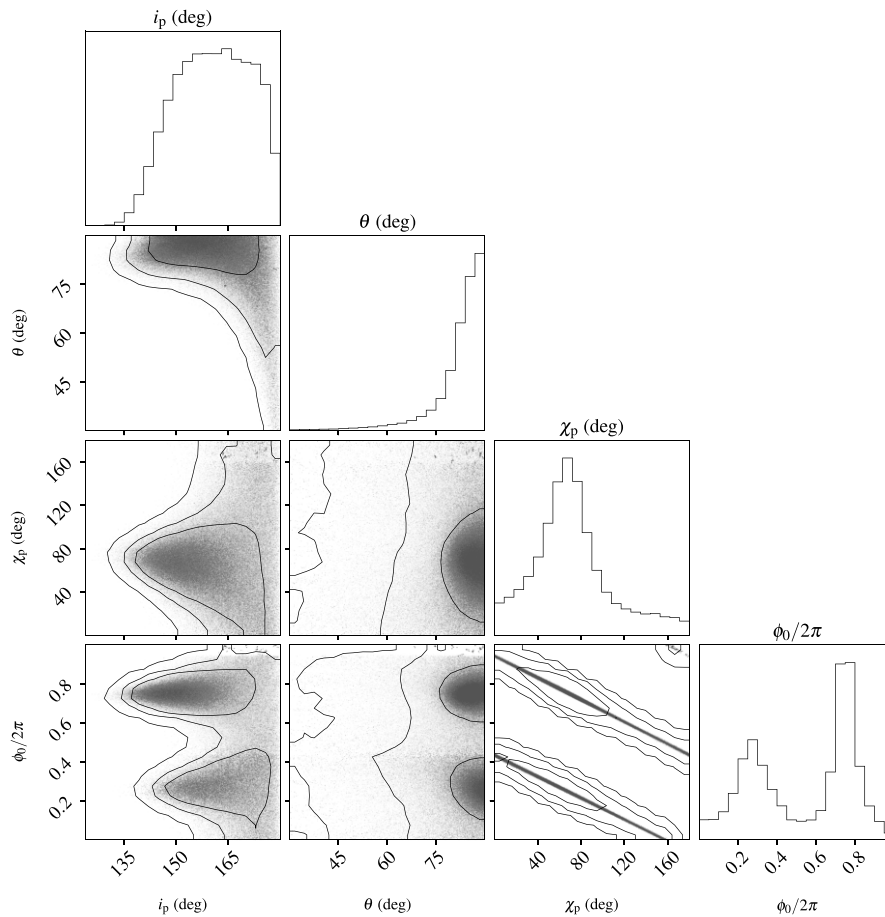
Figure 7. Corner plot of the posterior distribution for the RVM parameters using the PA dependence on the spin phase. The two-dimensional contours correspond to 68.27, 95.45, and 99.73 per cent confidence levels.

associated with a jump in mass density, and a large density range is present at the boundary between the cold atmosphere and the overheated upper layer. If the vacuum resonance density

$$\rho_V \approx 10^{-4} \, B_{12}^2 E_{keV}^2 \, \text{g cm}^{-3},$$ (1)

where B_{12} is the field strength in units of 10^{12} G and E_{keV} is the photon energy in keV (Lai & Ho 2003), falls into this density range, a polarization mode conversion is expected at the lower boundary of the overheated upper atmospheric layer. It has been shown previously that mode conversion in an overheated upper atmospheric layer leads to flux equalization in the two polarization modes, and a corresponding reduction in the linear PD (see Supplementary Materials in Doroshenko et al. 2022).

4.2 Constraints on the geometry

The PA makes two complete turns during the pulsation period (see Figs 3 and 5e). Polarization of X-ray photons with respect to the local direction of the magnetic field is conserved in the NS magnetosphere within the adiabatic radius $R_{ad} \approx 7.6 \times 10^6 \, B_{12}^{0.4} E_{keV}^{0.2}$ cm (Heyl & Shaviv 2000; González Caniulef et al. 2016). Thus, it is expected that the PA follows the projection of the magnetic field axis in the sky (or is perpendicular to this projection, depending on the polarization composition of the X-rays leaving the NS atmosphere). A full turn of the magnetic axis projection during the pulse period becomes possible under the condition

$$i_p < \theta, \quad \text{or} \quad i_p > 180^\circ - \theta,$$ (2)

where i_p is the pulsar spin inclination angle and θ is the magnetic obliquity, i.e. the angle between the rotation and the magnetic dipole. Interaction of the accretion flow with NS magnetosphere leads to the alignment of the NS spin, with the orbit on a time-scale (Biryukov & Abolmasov 2021)

$$\tau \approx 600 \, I_{45} \left(\frac{\dot{M}}{\dot{M}_{Edd}} \right)^{-6/7} \left(\frac{M}{M_\odot} \right)^{-9/7} \mu_{30}^{-2/7} \, \text{yr},$$ (3)

where I_{45} is the NS moment of inertia in units of 10^{45} g cm^2, $M_{Edd} \approx 1.6 \times 10^{18}$ g s^{-1} is the Eddington mass accretion rate onto a NS, and μ_{30} is the NS magnetic moment in units of 10^{30} G cm^3. For the observed mass accretion rate in X Persei and under the assumption of a surface magnetic field $B \sim 10^{13}$ G, we get the time-scale required for the alignment $\tau \sim 4 \times 10^5$ yr. The estimated time-scale of spin axis alignment is much smaller than the age reported for the optical companion in X Persei by Lyubimkov et al. (1997): $\sim 5 \times 10^6$ yr and sufficiently small to assume that the magnetic field of the NS has not experienced a significant decay (see Pons & Viganò 2019 for review and fig. 20 there). Thus, the rotational axis of the NS in X Persei is likely aligned with the orbital axis of the binary system. In this case, one would expect $i_p \sim i_{orb} \approx 30^\circ$, and the condition (2) can be easily satisfied.

To determine the geometry of X Persei, we follow the procedure applied earlier to Her X-1 (Doroshenko et al. 2022), Cen X-3 (Tsygankov et al. 2022), and GRO J1008−57 (Tsygankov et al. 2023), and fit the RVM (Radhakrishnan & Cooke 1969; Poutanen 2020) to the observed variation of the PA with phase ϕ. The PA χ is given by the expression

$$\tan(\chi - \chi_p) = \frac{-\sin\theta \, \sin(\phi - \phi_0)}{\sin i_p \cos\theta - \cos i_p \sin\theta \cos(\phi - \phi_0)},$$ (4)

where χ_p is the position angle of the pulsar's rotation axis (assuming that radiation escapes predominantly in the O-mode). We use

the affine-invariant Markov chain Monte Carlo ensemble sampler EMCEE package of PYTHON (Foreman-Mackey et al. 2013). All the parameters in equation (4) were left free. Because polarization is sensitive to the sense of rotation, the prior for the pulsar inclination i_p is [0° and 180°], with the probability density $\propto \sin i_p$. The inclination is constrained at $i_p = 162^\circ \pm 12^\circ$ at a 68 per cent confidence level and $i_p > 135^\circ$ at a 99 per cent confidence level. This is consistent with the orbital inclination $i_{orb} \in [26^\circ$ and $33^\circ]$ reported by Delgado-Martí et al. (2001), using the X-ray pulse arrival times and measured mass function (note that these constraints are equivalent to $i_{orb} \approx 150^\circ$ as the sense of rotation cannot be determined from such data). The probability distribution of the position angle χ_p has a broad peak at $\chi_{p,O} \approx 70^\circ$, with a 1σ width of about 30°. We note here that there is an alternative solution $\chi_p = \chi_{p,O} + 180^\circ = 250^\circ$, because only the orientation of the polarization plane can be measured. Furthermore, if radiation is dominated by the X-mode, then the pulsar spin orientation is $\chi_p = \chi_{p,X} = \chi_{p,O} \pm 90^\circ$.

The spin phase ϕ_0 when the closest pole is directed towards the observer has two maxima at $\phi_0/(2\pi) \approx 0.25$ and 0.75, because the two rotations of the PA are shifted by nearly exactly half a period. Finally, the magnetic obliquity tends to values close to 90°, with the lower limit being 75° at a 68 per cent confidence level. However, an orthogonal magnetic dipole in X Persei (i.e. $\theta \approx 90^\circ$), contradicts the behaviour of the normalized Stokes parameters q and u, during the pulse period (see Fig. 3): in the case of the orthogonal magnetic dipole, the behaviour of q and u parameters should duplicate itself in one and the other half of the spin period because after half a period, the NS arrives at the configuration that gives a similar set of Stokes parameters. Thus, a proper analysis of the data requires assumptions on the beam patterns in both polarization modes.

A sharp dip observed in the pulse profile at phase ~0.25 (Fig. 5), when the normal to one of the poles is close to the line of sight, can be related to an eclipse of the hotspot by the accretion stream above the NS surface. However, the mass accretion rate in X Persei is very low, and the optical thickness of the accretion stream above NS surface seems to be too small to support this hypothesis. Yet, the suggestion of a spot eclipse at this phase is also supported by observations of a sharp spike of the X-ray flux in the centre of the dip seen, for example, in the *Suzaku* data (Maitra et al. 2017) with the corresponding increase of the hardness ratio already observed with *EXOSAT* (Robba & Warwick 1989) and *Ginga* (Robba et al. 1996), which implies that here we are looking directly along the magnetic dipole axis.

Once the geometry of the pulsar is obtained from the RVM, we can now combine all the data to investigate the energy dependence of the polarimetric properties of X Persei in the phase-averaged data. Here we used all the data in the 2–8 keV *IXPE* band. To eliminate the effect of the PA rotation over pulse, the PAs were frozen at the predictions of the best-fitting RVM at a given phase (see equation 4 and Fig. 5e). We then performed a joint spectro-polarimetric fit of the data collected in all 14 phases, where instead of polconst model, we use the pollin model for each phase bin:

$$Q(E) = I(E)A(E)\cos(2\chi),$$
$$U(E) = I(E)A(E)\sin(2\chi),$$

where $A(E) = A_1 + A_{slope}(E - 1)$ with the photon energy E in keV and $I(E)$ is the spectral model of the absorbed power law, with the parameters fixed at the values presented in Table 2. The parameters of $A(E)$ were restricted to have the same values for all phases. As the result, we obtained the parameters $A_1 = -6.3 \pm 2.0$ per cent and $A_{slope} = 5.1 \pm 0.7$ per cent per keV. Such a dependence corresponds to zero PD at ~2.25 keV (which explains the non-

detection of polarization in the 2–3 keV band) and around 30 per cent at 8 keV. A negative value of the PD at 1 keV with the positive slope is mathematically equivalent to the rotation of the PA by 90° for photons at 1 keV relative to those at higher energies. However, from the available data, we cannot, of course, make any conclusion whether such a rotation actually happens below 2 keV. Using the F-test (standard `ftest` routine in XSPEC based on the $\Delta \chi^2$ value), we estimated the significance of the improvement of the fit with the `pollin` model, compared to `polconst` as 2×10^{-14}. It is worth mentioning that a similar behaviour of the PD increasing with energy was recently discovered in another XRP Vela X-1 (Forsblom et al. 2023), where the PD crosses zero within the *IXPE* range at ≈ 3.5 keV.

5 SUMMARY

The results of polarimetric studies of XRP X Persei can be summarized as follows:

(i) Linear polarization was not detected in the phase-averaged date from X Persei. However, the phase-resolved polarimetry revealed variable PD and PA. The energy-averaged PD in the 3–8 keV band reaches ~ 20 per cent, while the PA makes two complete revolutions during the pulsation period. The PD is detected to follow the variations of the X-ray energy flux during the observed pulse period (see panels a and d in Fig. 5). Similar behaviour of the flux and the PD was already reported in the low-luminosity XRP GRO J1008−57 (Tsygankov et al. 2023), and probably is a typical feature for XRPs at a luminosity well below the critical one.

(ii) The observed variations of the PA, making two full turns per spin period, become possible under the condition that the magnetic obliquity is larger than the inclination of the NS rotation axis. Application of the RVM to the data gives the following set of geometrical parameters: the inclination is constrained $i_{\rm p} = 162°$ $\pm 12°$ ($>135°$) at 68 (99) per cent confidence level, consistent with the orbital inclination reported in X Persei. The position angle has been determined as $70° \pm 30°$ or $250° \pm 30°$ (assuming that the observed photons were polarized in the O-mode), with alternative solutions rotated by $90°$, if radiation escapes in the X-mode. The magnetic obliquity has a preference towards $90°$ with the lower limit being $75°$ at a 68 per cent confidence level. High magnetic obliquity potentially makes X Persei the second discovered orthogonal rotator after GRO J1008−57.

(iii) Eliminating the effect of rotation of the PA with the pulse phase applying the predictions of the best-fitting RVM, a strong energy dependence of the PD was discovered, with the PD increasing from 0 at ~ 2 keV to 30 per cent at 8 keV, similarly to another XRP Vela X-1 (Forsblom et al. 2023).

(iv) The similarity of the determined NS inclination and the orbital inclination supports the hypothesis of a strong NS magnetic field in X Persei, which would make the relaxation period of the NS towards spin equilibrium and alignment with the orbital axis relatively fast, even under conditions of a rather low mass accretion rate.

(v) The low PD and its correlation with the X-ray flux during the pulse period are consistent with the expected inverse temperature profile in the NS atmosphere at low mass accretion rates. Under this condition, the beam pattern of X-ray radiation leaving the NS surface is expected to be suppressed along the normal to the surface. Thus, a smaller X-ray flux within the pulse period can be related to a smaller angle between the line of sight and the magnetic dipole.

DATA AVAILABILITY

The *IXPE* data used in this paper are publicly available in the HEASARC database.

REFERENCES

Arnaud K. A., 1996, in Jacoby G. H., Barnes J.eds, ASP Conf. Ser. Vol. 101, Astronomical Data Analysis Software and Systems V. Astron. Soc. Pac., San Francisco, p. 17

Bailer-Jones C. A. L., Rybizki J., Fouesneau M., Demleitner M., Andrae R., 2021, AJ, 161, 147

Baldini L. et al., 2021, Astropart. Phys., 133, 102628

Baldini L. et al., 2022, SoftwareX, 19, 101194

Basko M. M., Sunyaev R. A., 1976, MNRAS, 175, 395

Biryukov A., Abolmasov P., 2021, MNRAS, 505, 1775

Buccheri R. et al., 1983, A&A, 128, 245

Caiazzo I., Heyl J., 2021, MNRAS, 501, 109

Coburn W., Heindl W. A., Gruber D. E., Rothschild R. E., Staubert R., Wilms J., Kreykenbohm I., 2001, ApJ, 552, 738

Delgado-Martí H., Levine A. M., Pfahl E., Rappaport S. A., 2001, ApJ, 546, 455

Di Marco A. et al., 2023, AJ, 165, 143

Di Salvo T., Burderi L., Robba N. R., Guainazzi M., 1998, ApJ, 509, 897

Doroshenko V., Santangelo A., Kreykenbohm I., Doroshenko R., 2012, A&A, 540, L1

Doroshenko V. et al., 2022, Nature Astron., 6, 1433

Foreman-Mackey D., Hogg D. W., Lang D., Goodman J., 2013, PASP, 125, 306

Forsblom S. V. et al., 2023, ApJ, 947, L20

Gnedin Y. N., Pavlov G. G., 1974, Sov. J. Exp. Theor. Phys., 38, 903

González Caniulef D., Zane S., Taverna R., Turolla R., Wu K., 2016, MNRAS, 459, 3585

Harding A. K., Lai D., 2006, Rep. Prog. Phys., 69, 2631

Heyl J. S., Shaviv N. J., 2000, MNRAS, 311, 555

Kaminker A. D., Pavlov G. G., Shibanov I. A., 1983, Ap&SS, 91, 167

Kislat F., Clark B., Beilicke M., Krawczynski H., 2015, Astropart. Phys., 68, 45

Kong L.-D. et al., 2022, ApJ, 933, L3

Lai D., Ho W. C. G., 2003, ApJ, 588, 962

Lutovinov A., Tsygankov S., Chernyakova M., 2012, MNRAS, 423, 1978

Lyubimkov L. S., Rostopchin S. I., Roche P., Tarasov A. E., 1997, MNRAS, 286, 549

Maitra C., Raichur H., Pradhan P., Paul B., 2017, MNRAS, 470, 713

Meszaros P., 1992, High-energy radiation from magnetized neutron stars. Univ. Chicago Press, Chicago, p. 546

Meszaros P., Nagel W., 1985a, ApJ, 298, 147

Meszaros P., Nagel W., 1985b, ApJ, 299, 138

Meszaros P., Novick R., Szentgyorgyi A., Chanan G. A., Weisskopf M. C., 1988, ApJ, 324, 1056

Mushtukov A., Tsygankov S., 2022, in Bambi C., Santangelo A.eds, Handbook of X-ray and Gamma-ray Astrophysics. Springer, Singapore, p. preprint (arXiv:2204.14185)

Mushtukov A. A., Suleimanov V. F., Tsygankov S. S., Poutanen J., 2015, MNRAS, 447, 1847

Mushtukov A. A., Suleimanov V. F., Tsygankov S. S., Portegies Zwart S., 2021, MNRAS, 503, 5193

Nakajima M., Negoro H., Mihara T., Sugizaki M., Yatabe F., Makishima K., 2019, in Oskinova Lidia M., Bozzo GermanyEnrico, Bulik Tomasz, Gies Douglas R. eds, Proc. IAU Symp. 346, High-mass X-ray Binaries: Illuminating the Passage from Massive Binaries to Merging Compact Objects, Cambridge Univ. Press, p. 131

Pavlinsky M. et al., 2021, A&A, 650, A42

Pons J. A., Viganò D., 2019, Living Rev. Comput. Astrophys., 5, 3

Poutanen J., 2020, A&A, 641, A166

Radhakrishnan V., Cooke D. J., 1969, Astrophys. Lett., 3, 225

Reig P., Roche P., 1999, MNRAS, 306, 100

Robba N. R., Warwick R. S., 1989, ApJ, 346, 469

Robba N. R., Burderi L., Wynn G. A., Warwick R. S., Murakami T., 1996, ApJ, 472, 341

Soffitta P. et al., 2021, AJ, 162, 208

Sokolova-Lapa E. et al., 2021, A&A, 651, A12

Staubert R. et al., 2019, A&A, 622, A61

Strohmayer T. E., 2017, ApJ, 838, 72

Suleimanov V. F., Poutanen J., Werner K., 2018, A&A, 619, A114

Suleimanov V. F., Mushtukov A. A., Ognev I., Doroshenko V. A., Werner K., 2022, MNRAS, 517, 4022

Sunyaev R. et al., 2021, A&A, 656, A132

Tsygankov S. S., Mushtukov A. A., Suleimanov V. F., Doroshenko V., Abolmasov P. K., Lutovinov A. A., Poutanen J., 2017, A&A, 608, A17

Tsygankov S. S., Rouco Escorial A., Suleimanov V. F., Mushtukov A. A., Doroshenko V., Lutovinov A. A., Wijnands R., Poutanen J., 2019a, MNRAS, 483, L144

Tsygankov S. S., Doroshenko V., Mushtukov A. A., Suleimanov V. F., Lutovinov A. A., Poutanen J., 2019b, MNRAS, 487, L30

Tsygankov S. S. et al., 2022, ApJ, 941, L14

Tsygankov S. S. et al., 2023, A&A, 675, A48

Wang Y. M., Frank J., 1981, A&A, 93, 255

Weisskopf M. C. et al., 2022, J. Astron. Telesc. Instrum. Syst., 8, 026002

White N. E., Mason K. O., Sanford P. W., Murdin P., 1976, MNRAS, 176, 201

Wilms J., Allen A., McCray R., 2000, ApJ, 542, 914

Yatabe F., Makishima K., Mihara T., Nakajima M., Sugizaki M., Kitamoto S., Yoshida Y., Takagi T., 2018, PASJ, 70, 89

Zel'dovich Y. B., Shakura N. I., 1969, SvA, 13, 175

[1]*Astrophysics, Department of Physics, University of Oxford, Denys Wilkinson Building, Keble Road, Oxford OX1 3RH, UK*

[2]*Leiden Observatory, Leiden University, NL-2300RA Leiden, the Netherlands*

[3]*Department of Physics and Astronomy, FI-20014 University of Turku, Finland*

[4]*Institut für Astronomie und Astrophysik, Universität Tübingen, Sand 1, D-72076 Tübingen, Germany*

[5]*Department of Astronomy, Saint Petersburg State University, Saint-Petersburg 198504, Russia*

[6]*Space Research Institute of the Russian Academy of Sciences, Profsoyuznaya Str. 84/32, Moscow 117997, Russia*

[7]*INAF Istituto di Astrofisica e Planetologia Spaziali, Via del Fosso del Cavaliere 100, 00133 Roma, Italy*

[8]*Department of Physics and Astronomy, University of British Columbia, Vancouver, BC V6T 1Z1, Canada*

[9]*INAF Osservatorio Astronomico di Roma, Via Frascati 33, I-00040 Monte Porzio Catone (RM), Italy*

[10]*Institut de Recherche en Astrophysique et Planétologie, UPS-OMP, CNRS, CNES, 9 avenue du Colonel Roche, BP 44346 31028, Toulouse CEDEX 4, France*

[11]*International Space Science Institute, Hallerstrasse 6, CH-3012 Bern, Switzerland*

[12]*Max Planck Institute for Astrophysics, Karl-Schwarzschild-Str 1, D-85741 Garching, Germany*

[13]*Instituto de Astrofísica de Andalucía-CSIC, Glorieta de la Astronomía s/n, E-18008 Granada, Spain*

[14]*INAF Osservatorio Astronomico di Roma, Via Frascati 33, I-00078 Monte Porzio Catone (RM), Italy*

[15]*Space Science Data Center, Agenzia Spaziale Italiana, Via del Politecnico snc, I-00133 Roma, Italy*

[16]*INAF – Osservatorio Astronomico di Cagliari, via della Scienza 5, I-09047 Selargius (CA), Italy*

[17]*Istituto Nazionale di Fisica Nucleare, Sezione di Pisa, Largo B. Pontecorvo 3, I-56127 Pisa, Italy*

[18]*Dipartimento di Fisica, Università di Pisa, Largo B. Pontecorvo 3, I-56127 Pisa, Italy*

[19]*NASA Marshall Space Flight Center, Huntsville, AL 35812, USA*

[20]*Dipartimento di Matematica e Fisica, Università degli Studi Roma Tre, Via della Vasca Navale 84, I-00146 Roma, Italy*

[21]*Istituto Nazionale di Fisica Nucleare, Sezione di Torino, Via Pietro Giuria 1, I-10125 Torino, Italy*

[22]*Dipartimento di Fisica, Università degli Studi di Torino, Via Pietro Giuria 1, I-10125 Torino, Italy*

[23]*INAF Osservatorio Astrofisico di Arcetri, Largo Enrico Fermi 5, I-50125 Firenze, Italy*

[24]*Dipartimento di Fisica e Astronomia, Università degli Studi di Firenze, Via Sansone 1, I-50019 Sesto Fiorentino (FI), Italy*

[25]*Istituto Nazionale di Fisica Nucleare, Sezione di Firenze, Via Sansone 1, I-50019 Sesto Fiorentino (FI), Italy*

[26]*ASI - Agenzia Spaziale Italiana, Via del Politecnico snc, I-00133 Roma, Italy*

[27]*Science and Technology Institute, Universities Space Research Association, Huntsville, AL 35805, USA*

[28]*Istituto Nazionale di Fisica Nucleare, Sezione di Roma 'Tor Vergata', Via della Ricerca Scientifica 1, I-00133 Roma, Italy*

[29]*Department of Physics and Kavli Institute for Particle Astrophysics and Cosmology, Stanford University, Stanford, California 94305, USA*

[30]*Astronomical Institute of the Czech Academy of Sciences, Boční II 1401/1, CZ-14100 Praha 4, Czech Republic*

[31]*RIKEN Cluster for Pioneering Research, 2-1 Hirosawa, Wako, Saitama 351-0198, Japan*

[32]*California Institute of Technology, Pasadena, CA 91125, USA*

[33]*Yamagata University,1-4-12 Kojirakawa-machi, Yamagata-shi 990-8560, Japan*

[34]*Osaka University, 1-1 Yamadaoka, Suita, Osaka 565-0871, Japan*

[35]*International Center for Hadron Astrophysics, Chiba University, Chiba 263-8522, Japan*

[36]*Institute for Astrophysical Research, Boston University, 725 Commonwealth Avenue, Boston, MA 02215, USA*

[37]*Department of Astrophysics, St. Petersburg State University, Universitetsky pr. 28, Petrodvoretz, 198504 St. Petersburg, Russia*

[38]*University of New Hampshire, Department of Physics & Astronomy and Space Science Center, 8 College Rd, Durham, NH 03824, USA*

[39]*Physics Department and McDonnell Center for the Space Sciences, Washington University in St. Louis, St. Louis, MO 63130, USA*

[40] *Finnish Centre for Astronomy with ESO, FI-20014 University of Turku, Finland*

[41] *Istituto Nazionale di Fisica Nucleare, Sezione di Napoli, Strada Comunale Cinthia, I-80126 Napoli, Italy*

[42] *Université de Strasbourg, CNRS, Observatoire Astronomique de Strasbourg, UMR 7550, F-67000 Strasbourg, France*

[43] *MIT Kavli Institute for Astrophysics and Space Research, Massachusetts Institute of Technology, 77 Massachusetts Avenue, Cambridge, MA 02139, USA*

[44] *Graduate School of Science, Division of Particle and Astrophysical Science, Nagoya University, Furo-cho, Chikusa-ku, Nagoya, Aichi 464-8602, Japan*

[45] *Hiroshima Astrophysical Science Center, Hiroshima University, 1-3-1 Kagamiyama, Higashi-Hiroshima, Hiroshima 739-8526, Japan*

[46] *University of Maryland, Baltimore County, Baltimore, MD 21250, USA*

[47] *NASA Goddard Space Flight Center, Greenbelt, MD 20771, USA*

[48] *Center for Research and Exploration in Space Science and Technology, NASA/GSFC, Greenbelt, MD 20771, USA*

[49] *Department of Physics, The University of Hong Kong, Pokfulam, Hong Kong*

[50] *Department of Astronomy and Astrophysics, Pennsylvania State University, University Park, PA 16802, USA*

[51] *Université Grenoble Alpes, CNRS, IPAG, F-38000 Grenoble, France*

[52] *Center for Astrophysics, Harvard & Smithsonian, 60 Garden St, Cambridge, MA 02138, USA*

[53] *INAF Osservatorio Astronomico di Brera, Via E. Bianchi 46, I-23807 Merate (LC), Italy*

[54] *Dipartimento di Fisica e Astronomia, Università degli Studi di Padova, Via Marzolo 8, I-35131 Padova, Italy*

[55] *Dipartimento di Fisica, Università degli Studi di Roma 'Tor Vergata', Via della Ricerca Scientifica 1, I-00133 Roma, Italy*

[56] *Department of Astronomy, University of Maryland, College Park, Maryland 20742, USA*

[57] *Mullard Space Science Laboratory, University College London, Holmbury St Mary, Dorking, Surrey RH5 6NT, UK*

[58] *Anton Pannekoek Institute for Astronomy & GRAPPA, University of Amsterdam, Science Park 904, NL-1098 XH Amsterdam, the Netherlands*

[59] *Guangxi Key Laboratory for Relativistic Astrophysics, School of Physical Science and Technology, Guangxi University, Nanning 530004, China*

This paper has been typeset from a TEX/LATEX file prepared by the author.